

High Brightness, Highly Directional Organic Light-Emitting Diodes as Light Sources for Future Light-Amplifying Prosthetics in the Optogenetic Management of Vision Loss

Sabina Hillebrandt, Changmin Keum, Yali Deng, Joël Chavas, Charlie Galle, Thomas Hardin, Francesco Galluppi, and Malte C. Gather*

Optogenetic control of retinal cells transduced with light-sensitive channelrhodopsins can enable restoration of visual perception in patients with vision loss. However, a light intensity orders of magnitude higher than ambient light conditions is required to achieve robust cell activation. Relatively bulky wearable light amplifiers are currently used to deliver sufficient photon flux ($>10^{16}$ photons/cm²/s in a $\pm 10^\circ$ emission cone) at a suitable wavelength (e.g., 600 nm for channelrhodopsin ChrimsonR). Here, ultrahigh brightness organic light-emitting diodes (OLEDs) with highly directional emission are developed, with the ultimate aim of providing high-resolution optogenetic control of thousands of retinal cells in parallel from a compact device. The orange-emitting phosphorescent OLEDs use doped charge transport layers, generate narrowband emission peaking at 600 nm, and achieve a luminance of 684 000 cd m⁻² at 15 V forward bias. In addition, tandem-stack OLEDs with a luminance of 1 152 000 cd m⁻² and doubled quantum efficiency are demonstrated, which greatly reduces electrical and thermal stress in these devices. At the photon flux required to trigger robust neuron firing in genetically modified retinal cells and when using heat sinking and realistic duty cycles (20% at 12.5 Hz), the tandem-stack OLEDs therefore show a greatly improved half-brightness lifetime of 800 h.

1. Introduction

Human sensing and behavior are dominated by visual stimuli, thus there is a strong demand for treatments for vision loss, including genetic therapies and visual implants.^[1–3] Monogenetic diseases can be treated by transducing the healthy version of the defective gene sequence into the affected cells.^[4,5] However, for heterogeneous diseases, genetically modifying the remaining functional cells to add the required function may be more beneficial. Optogenetics is an increasingly popular method in neuroscience, in which neurons are genetically modified, e.g., through viral transduction, to express a light-sensitive ion channel. Exposure to light then allows targeted stimulation or silencing of these neurons.^[6–8] For a heterogeneous disease like retinitis pigmentosa, one promising route is to use optogenetics to modify retinal ganglion cells (RGCs) with light-sensitive channelrhodopsins (ChRs).^[9,10] As illustrated in **Figure 1a**, this approach can enable external light stimulation of RGCs in the retina and thus facilitate basic perception of light.^[2,11]

Despite continuous improvements to optogenetics and to ChRs in particular, the modified RGCs are less light sensitive than the endogenous opsins in the rods and cones of the human retina, and consequently higher light intensities than natural environmental conditions are required to stimulate the modified RGCs. Therefore, visual prosthetics that act as a light amplifier are an essential part of this approach.^[12,13]

Typically, a minimum optical power density in the range of 10 to 100s of $\mu\text{W mm}^{-2}$ is required to photostimulate neurons through genetically introduced opsins. With the recent development of red-shifted ChRs, the delivery of such high light intensities into the eye without causing significant photodamage has come into reach.^[2,14–17] The ChR ChrimsonR is a suitable candidate in this context due to its red-shifted action spectrum and fast recovery kinetics.^[18] Recent studies in non-human primates reported that up to 7000 RGCs mm⁻² can be transfected with ChrimsonR-tdT and that 600 nm light reliably activates those RGCs at photon densities of 10^{16} photons/cm²/s, which is three orders of magnitude higher than the stimulation provided by bright daylight.^[19] Compared to electrode-based local


S. Hillebrandt, C. Keum, Y. Deng, M. C. Gather
Organic Semiconductor Centre
SUPA

School of Physics and Astronomy
University of St Andrews
North Haugh, St Andrews KY16 9SS, UK
E-mail: mcg6@st-andrews.ac.uk

J. Chavas, C. Galle, T. Hardin, F. Galluppi
GenSight Biologics S.A.
74, rue du Faubourg Saint-Antoine, Paris 75012, France

M. C. Gather
Humboldt Centre for Nano- and Biophotonics
Department of Chemistry
University of Cologne
Greinstr. 4–6, 50939 Köln, Germany

© 2022 The Authors. Advanced Optical Materials published by Wiley-VCH GmbH. This is an open access article under the terms of the Creative Commons Attribution License, which permits use, distribution and reproduction in any medium, provided the original work is properly cited.

 The ORCID identification number(s) for the author(s) of this article can be found under <https://doi.org/10.1002/adom.202200877>.

DOI: 10.1002/adom.202200877

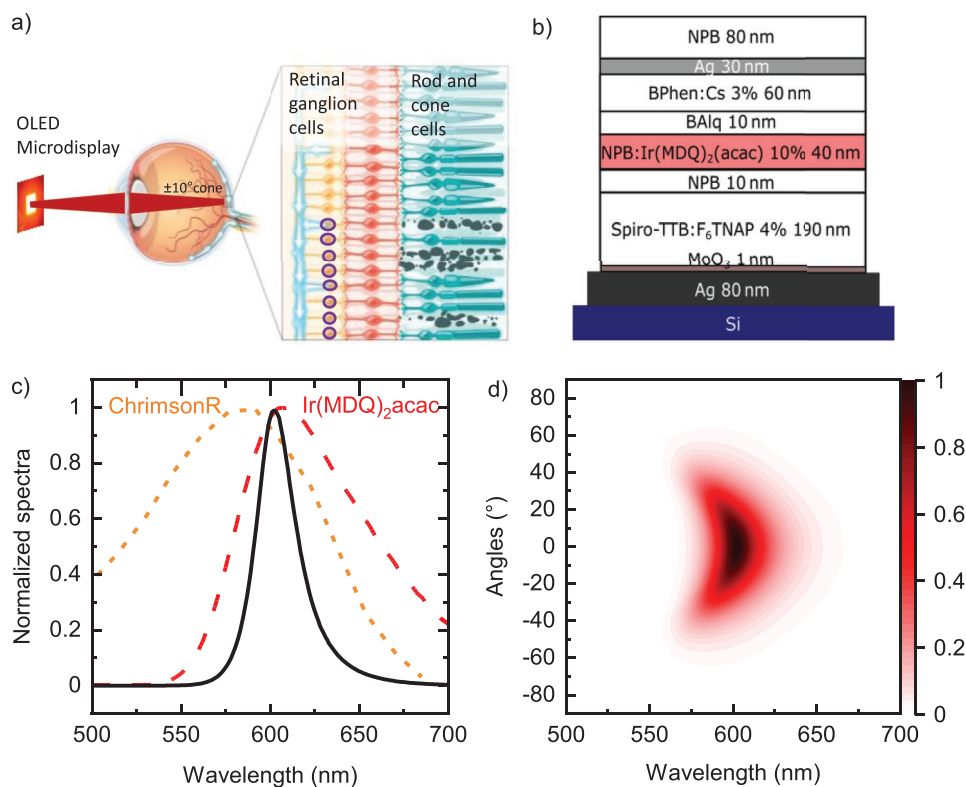


Figure 1. a) Sketch of the combination of genetically modified RGCs (indicated by purple circles) and an OLED microdisplay in front of the eye generating the light required to achieve robust photostimulation. b) Architecture of the single-stack top-emitting microcavity p-i-n OLED on a silicon substrate. Doping concentrations are given in weight percent. c) Simulated emission spectrum of the single-stack OLED in the forward direction (solid line), intrinsic phosphorescence spectrum of the emitter Ir(MDQ)₂acac used in this device (dashed line), and action spectrum of the channelrhodopsin ChrimsonR (short dashed line).^[18] d) Simulated emission intensity versus angle and wavelength for the single-stack microcavity OLED. All spectra are normalized to maximum spectral intensity.

stimulation, the fact that light-amplifying prosthetics can be worn externally and do not need to be implanted still represents a major advantage in terms of biocompatibility.

The ideal light-amplifying prosthetics are wearable, lightweight, and compact, and are able to deliver an amplified image of the surroundings to the retina. Microprojectors based on digital micromirror devices (DMDs) are generally used to achieve this objective in current clinical trials.^[20] However, this strategy requires a high-power inorganic LED and an optical system with multiple lenses and mirrors or prisms, which add weight to the system and reduce energy efficiency. A prominent alternative is the use of a microdisplay combined with a simple 1:1 projection system to relay the image from the microdisplay onto the retina.

Due to its geometry, the eye only accepts light from the $\pm 10^\circ$ cone around the optical axis. When using a 1:1 projection, this means that only the light emanating from the central $\pm 10^\circ$ emission cone of a light source is harvested. Therefore, 10^{16} photons/cm²/s must be generated within this $\pm 10^\circ$ emission cone in order to generate reliable neuronal responses.^[2,11,19,21] Various light sources such as fiber optics, LEDs and DMDs have been used for defined stimulation of neurons.^[11,21–23] Recent advances in LED array fabrication technology are particularly promising for wearable devices, though major challenges still remain, particularly related to upscaling of the technology,

the integration of suitable backplane driver electronics, and color-tuning.^[24,25] Specifically, integrating conventional LED technology (typically based on GaN) with the silicon based, complementary metal-oxide-semiconductor (CMOS) backplane driver chips required to allow addressing of each pixel in the array remains very challenging. Lattice matching constraints prevent monolithic integration and alternatives, like face-to-face bonding of thinned GaN/InGaN μ LEDs to the CMOS substrate, have low yield and resolution.

Organic light-emitting diodes (OLEDs) represent a thin, lightweight, spectrally tunable, and rapidly switchable technology that is compatible with nearly any substrate.^[26–28] OLED technology has enabled the realization of high-resolution, portable, and low power-consumption displays for mobile phones and TVs.^[29,30] Integration of top-emitting OLEDs with CMOS backplane driver chips has allowed the production of displays and sensors with high fill factors and micrometer-sized, direct emissive-element pixels.^[31–34] However, compared to their inorganic counterparts, the limited stability of OLEDs at high brightness remains an open research challenge.

In this publication, we present a feasibility study of whether orange-emitting p-i-n OLEDs can be made that provide sufficient brightness, directionality, and stability to be useful for integration on CMOS chips and thus for the fabrication of microdisplays that act as light-amplifying prosthetics for

external light stimulation of genetically modified, ChrimsonR-expressing RGCs in the retina. We fabricated top-emitting devices on silicon substrates that act as surrogates for future implementation on silicon CMOS chips. The optical properties of the OLEDs and their microcavity (MC) structures were first simulated and then experimentally optimized. Our orange phosphorescent OLEDs achieve high brightness, with an emission spectrum adjusted to the action spectrum of ChrimsonR, while exhibiting highly directional sub-Lambertian emission. The number of photons the OLEDs delivered into the $\pm 10^\circ$ forward emission cone is around 10% of the overall emission, significantly higher than what can be achieved for conventional Lambertian emission. First, we present OLEDs with a single-stack architecture that deliver a photon flux of 3×10^{16} photons/cm²/s at 10 V in the $\pm 10^\circ$ cone, which corresponds to the flux required to generate reliable neuronal responses in the eye. We then improve our design to a monocolored tandem device, which reaches the same photon flux at less than half the current density. Using a combination of heat sinking and pulsed driving, our OLEDs achieve a half-brightness lifetime of 21 h for the single stack and 800 h for the tandem stack when operated at a photon flux of 3×10^{16} photons/cm²/s. Tandem stacking significantly increased the device efficiency, and enabled a peak luminance of 1 152 000 cd m⁻² and total photon flux of over 8×10^{17} photons/cm²/s (3 mW mm^{-2}) to be achieved, without showing signs of immediate device failure. Therefore, our study demonstrates how OLEDs integrated on silicon CMOS can be specifically adjusted for the high brightness requirements of optogenetic stimulation and light-amplifying prosthetics.

2. Results

2.1. Concept and Optical Simulations

The implementation of OLEDs on silicon substrates requires the use of top-emitting architectures, which result in a MC structure, as illustrated in Figure 1b. The structure of our orange phosphorescent OLEDs consists of a thick silver layer as a bottom anode contact, followed by a 1 nm thick MoO₃ interlayer, and a p-doped hole transport layer (HTL, 190 nm) of Spiro-TTB:F₆TNAP. NPB serves as an electron blocking layer (EBL, 10 nm) and as a host material for the emitter Ir(MDQ)₂acac in the emission layer (EML, 40 nm). The hole blocking layer (HBL, 10 nm) is BaIq₂, with the subsequent electron transport layer (ETL, 60 nm) consisting of Cs-doped BPhen. The device is completed with a semitransparent, 30 nm thick, silver top cathode, and a dielectric capping layer (NPB, 80 nm) on top of the silver cathode to increase the outcoupling efficiency.^[35]

To facilitate high-brightness operation, the OLEDs contain doped transport layers (HTL and ETL), which allow ohmic charge injection and help to reduce ohmic losses across the charge transport layers of the devices.^[36,37] The thicknesses of the HTL and ETL were optimized such that the EML lies in the second maximum of the electric field distribution relative to the anode layer. This leads to a loss in external quantum efficiency (EQE) for the orange phosphorescent OLED stack, while bringing the benefits of a higher forward luminance and narrower emission cone (see Figure S1b, Supporting Information)

with better stability, as previously reported.^[35,38,39] MoO₃ was used as an interface layer to improve the thermal stability of the device, which is required for compatibility with thin film encapsulation and for operation at high power.^[40]

Transfer matrix (TM) simulations were performed to optimize the emission wavelength of the MC OLED and determine the device architecture.^[41] The emission wavelength can be tuned by changing the thickness—and thus the resonance wavelength—of the MC to achieve the most efficient overlap conditions between the Ir(MDQ)₂acac emission spectrum and the action spectrum of ChrimsonR.^[19] On one hand, to achieve the highest possible EQE, the MC resonance should coincide with the peak of the Ir(MDQ)₂acac emission spectrum (dashed line in Figure 1c). On the other hand, the response of the light-sensitive ChR is generated by the overlap between the OLED emission spectrum and ChR action spectrum. Thus, blue-shifting the MC resonance too far will increase the overlap with the action spectrum and photon efficiency but significantly decrease the outcoupling efficiency, and vice versa. Here, we found that tuning the OLED stack for emission at 600 nm provides the optimum overlap between the emitter spectrum of Ir(MDQ)₂acac and the action spectrum of the ChR (Figure S1 and Table S3, Supporting Information, for further details). The simulated emission spectra in Figure 1d show that highly forward directed emission can be achieved for this case. This comes at the cost of some angular dependency on the emission wavelength, which is typical for MC OLEDs, but is not considered to cause an issue for the intended application.

To reduce complexity and allow future transfer of our device architecture to the widest possible range of substrates, we decided not to use additional outcoupling structures, even though these may potentially further increase the outcoupling efficiency and directionality.^[42,43]

2.2. High Power and High Brightness

Next, OLEDs with an active area of $2 \times 2 \text{ mm}^2$ were produced using the optimized stack architecture obtained from our optical simulations. As expected from the simulations, the measured emission spectra of these OLEDs exhibit a peak emission wavelength of 600 nm and a spectral full width at half maximum (FWHM) of 18 nm (Figure 2a). The MC resonance exhibits highly forward-directed sub-Lambertian emission (Figure 2b, black line, and Figure 2d) with around 10% of the total generated light emitted into the $\pm 10^\circ$ forward emission cone, which represents a threefold increase in directionality compared to Lambertian emission (compare Table S2, Supporting Information). Increasing the thickness of the Ag top contact improves the conductivity and strengthens the MC effect and thus directs more light in the forward direction, which is beneficial for the application of our OLED in light-amplifying prosthetics. However, the loss in transparency on increasing the thickness of Ag also reduces the outcoupling efficiency. The device with a 30 nm thick semitransparent top cathode exhibits the optimal current efficiency and brightness, while still providing high directionality (see Figure S3, Supporting Information).

Ultimately, for excitation of single RGCs in the retina, much smaller pixels (than tested here) will be necessary, thus it is

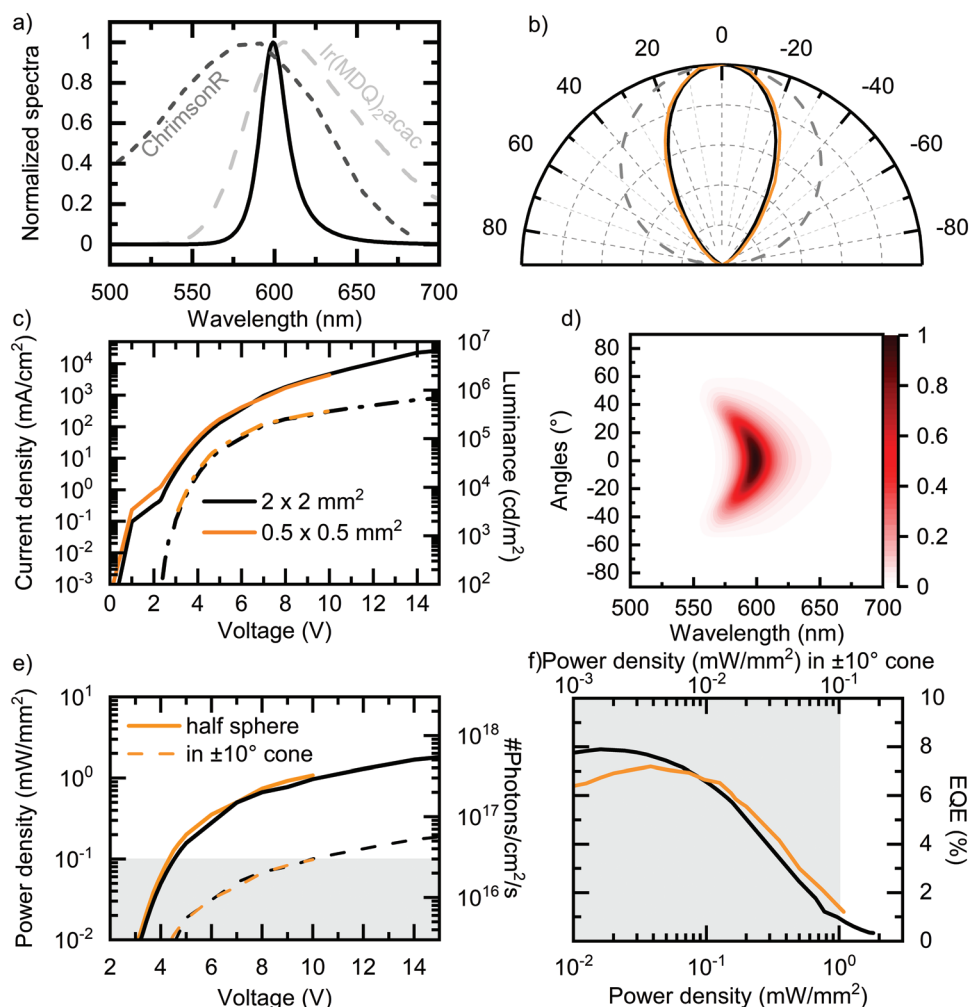


Figure 2. Experimental data of second-order devices with a 190 nm thick HTL, 60 nm thick ETL and 30 nm thick Ag top contact. a) Electroluminescence spectrum in the forward direction for the device (black), compared to the intrinsic phosphorescence spectrum of Ir(MDQ)₂acac (gray dashed line) and the action spectrum of ChrimsonR (gray dotted line). b) Spectrally integrated radiant intensity of a 2 × 2 mm² device (black line) and a 0.5 × 0.5 mm² device (orange line) as a function of angle, normalized to the intensity in the forward direction. The dashed line indicates Lambertian emission. c) Current density (solid lines) and forward luminance (dashed lines) as a function of the applied voltage for the 2 × 2 mm² and 0.5 × 0.5 mm² devices. d) Angle-resolved electroluminescence emission intensity measured across all angles and wavelengths for the optimized stack. All spectra are normalized to the maximum spectral intensity. e) Left axis: power density emitted into the forward half sphere (solid lines) and the forward ±10° emission cone (dashed lines), considering the actual device emission profile of the devices shown in b. Right axis: the corresponding photon density is shown for comparison. The gray box marks the threshold above which stable optical stimulation of the genetically modified RGCs is expected. f) External quantum efficiency plotted against power density (in the ±10° emission cone). All device characteristics are calculated by taking their non-Lambertian emission profile into account.^[44]

important to investigate if the characteristics—especially the angular emission of the OLED—change when the pixel size is reduced. Therefore, 0.5 × 0.5 mm² pixels were also fabricated; their angle-dependent emission spectrum (Figure 2b, orange lines) coincides with the data for the 2 × 2 mm² devices.

In order to achieve robust activation of genetically modified RGCs while minimizing photodamage to the surrounding retinal tissue, the OLEDs would ultimately be operated at high power, yet in pulsed mode.^[45–47] However, the dissipation of parasitic heat produced during device operation, even in pulsed operating mode, can be problematic. Therefore, a copper heat sink was attached to the backside of the OLED to improve device stability. With this modification, the 2 × 2 mm² devices

exhibit a luminance of 368 000 and 684 000 cd m⁻² at 10 V and 15 V, respectively (Figure 2c). The emission spectra do not show any significant changes at different voltages and luminance levels (Figure S4, Supporting Information) and the peak emission within the ±10° cone experiences a minimal shift of less than 2 nm (Figure S7, Supporting Information).

While quoting luminance in cd m⁻² is useful for comparison with the existing literature on OLEDs, these values take the photopic response of the healthy human eye into account. To compare the amount of light produced by different OLEDs in the context of their use in optogenetics, it is more useful to look at their optical power density and their photon efficiency with respect to the action spectrum of ChrimsonR, which deviates

substantially from the photopic response spectrum of the healthy human eye. The optical power densities of both devices for emission into the entire half sphere and into the $\pm 10^\circ$ emission cone are shown in Figure 2e. While optical power density values of around 1.0 mW mm^{-2} are reached when considering emission into the entire half sphere, restricting light collection to the relevant $\pm 10^\circ$ emission cone reduces this value by about 10-fold to an effective optical power density of around 0.1 mW mm^{-2} . The photon flux produced by each device can be calculated based on the average photon energy and is plotted as a guide on the right y-axis of Figure 2e. At 10 V, our devices reach a photon flux of $3 \times 10^{16} \text{ ph/cm}^2/\text{s}$ in the $\pm 10^\circ$ cone, which is sufficient to provoke robust neuronal stimulation in genetically modified RGCs. The voltage required to reach these levels of photon flux is considerably higher than voltages typically used in CMOS circuitry. However, recent advances in the CMOS and lateral diffusion MOS (LDMOS) design^[48–50] allow the creation of integrated submicron dimensions and circuits with sufficient voltage and power to realize high-resolution, ultrahigh brightness OLED microdisplays.

2.3. Monocolored Tandem Stack

The high current and charge carrier density in our phosphorescent OLEDs under the conditions required for robust neural

stimulation result in a high triplet state density, and thus induce strong efficiency roll-off due to triplet-triplet and triplet-polaron annihilation.^[36,37,51] At 10 V, the EQE reduces to about 1.0% for the $2 \times 2 \text{ mm}^2$ device and 1.2% for the $0.5 \times 0.5 \text{ mm}^2$ device. In addition to reducing the efficiency, nonradiative processes stress the device and accelerate degradation.^[52,53] To reduce the efficiency roll-off, we designed monocolored tandem devices, in which each injected electron generates two photons, thus theoretically halving the stress on each emission layer and doubling the quantum efficiency.

The structure of our monocolored tandem device is shown in Figure 3a. The center piece of the tandem OLED is the charge generation layer, which is required to ensure charge carrier injection into both EML layers. Charge generation layers usually consist of a high and a low work function material, including (electrically doped) organic semiconductors and ultrathin metals or transition metal oxides.^[54,55] In this study, we implemented a 10 nm thick MoO_3 layer to generate charges at the interface with the Spiro-TTB: F_6TNAP due to band alignment of the HOMO and LUMO levels. The individual stacks are designed as symmetrical first-order devices (HTL/ETL 40 nm/50 nm). Thus, the overall thickness of the tandem device is comparable with that of the second-order single structure, which reduces the risk of thermal degradation due to insufficient vertical heat dissipation.

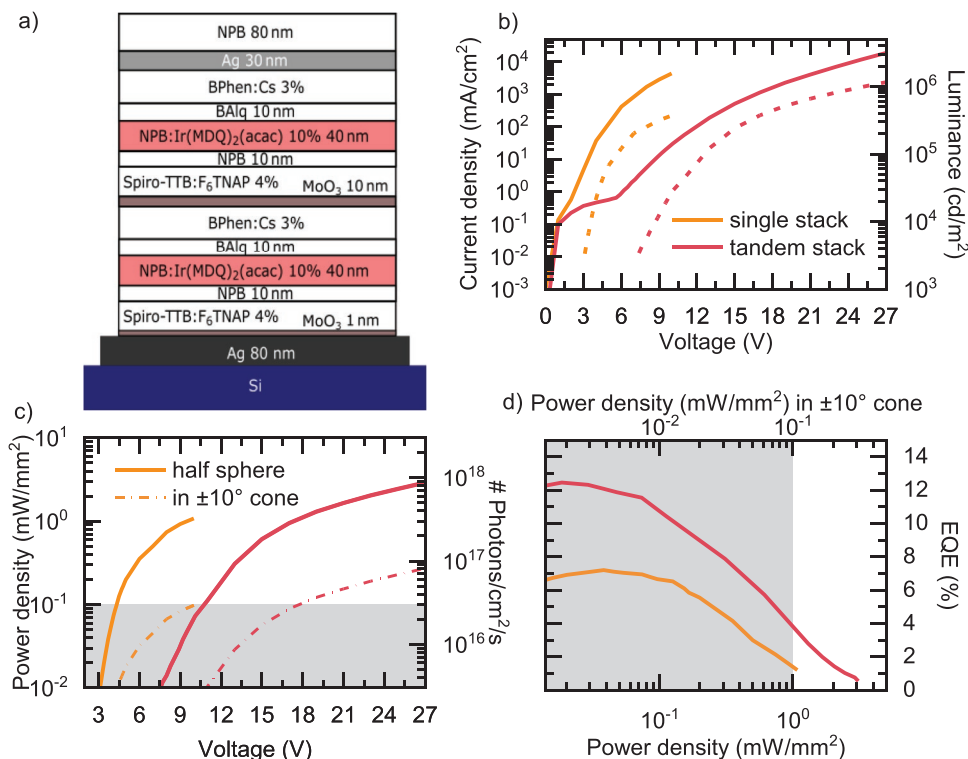


Figure 3. a) Schematic of the tandem-stack architecture on the silicon substrate. Doping concentrations are given in weight percent. Internal charge generation occurs at the interface of the 10 nm thick MoO_3 layer and Spiro-TTB: F_6TNAP . b) Current density (solid lines) and forward luminance (dashed lines) as a function of the applied voltage for the $0.5 \times 0.5 \text{ mm}^2$ single (orange) and tandem (red) devices. c) Left axis: power density emitted into the forward half sphere (solid lines) and the $\pm 10^\circ$ emission cone (dashed lines), considering the actual emission profiles of the devices. Right axis: corresponding photon flux. The gray box marks the threshold above which stable optical stimulation of genetically modified RGCs is expected. d) External quantum efficiency plotted against the optical power density emitted into the forward half sphere (bottom axis) and within the $\pm 10^\circ$ emission cone (top axis).

Figure 3b–d compares the characteristics of the $0.5 \times 0.5 \text{ mm}^2$ single-stack and tandem-stack devices. The characteristics of the $2 \times 2 \text{ mm}^2$ devices are shown in Figure S6 (Supporting Information). The current density–voltage–luminance (*JVL*) characteristics in Figure 3b show that, as expected, the tandem cells need a higher voltage but lower current density to generate a similar brightness as the single device. A luminance of $368\,000 \text{ cd m}^{-2}$ can be generated at 10 V and 4.2 A cm^{-2} by the single stack, while the tandem stack reaches this luminance at 17 V and 1.4 A cm^{-2} . A luminance of over $1152\,000 \text{ cd m}^{-2}$ can be achieved by the tandem OLEDs at 27 V and 19 A cm^{-2} , without causing acute device degradation.

The power density emitted into the entire half sphere reaches a maximum of 3 mW mm^{-2} at 27 V, which corresponds to a total photon flux of $8 \times 10^{17} \text{ photons/cm}^2/\text{s}$ and a flux of $8 \times 10^{16} \text{ photons/cm}^2/\text{s}$ in the $\pm 10^\circ$ cone (Figure 3c, angle-resolved emission Figure S6e, Supporting Information). The power density needed to evoke a signal in genetically modified RGCs through the restricted acceptance angle of the eye (0.1 mW mm^{-2} and $>10^{16} \text{ photons/cm}^2/\text{s}$ in the $\pm 10^\circ$ emission cone) is reached at 17.5 V. At this forward bias, the device EQE is still 3.6%. Compared to the single device, the EQE at high brightness is more than doubled (Figure 3d and Figure S6 and Table S2, Supporting Information), which confirms that the charge generation interface is working and that both cells in the tandem stack efficiently contribute to the emission generated by the tandem OLED.

2.4. Stability

Apart from delivering sufficient photon flux to the retina to trigger a robust response in genetically modified RGCs, OLEDs must also exhibit sufficient stability under high brightness operation to enable their use in a light-amplifying prosthetic. Our use of p–i–n stacks, small pixel areas, silicon substrates with excellent heat conductivity, and application of an external

heat sink all reduce Joule heating, even when relatively large amounts of power are dissipated in our devices. However, the high charge carrier density and highly confined recombination zone are still expected to cause stress on the organic materials and may result in rapid degradation of device performance.^[52,56–59]

We performed stability measurements for both the single- and tandem-stack devices by recording their optical power density and current density during extended pulsed operation (12.5 Hz, 20% duty cycle), with the preset voltage chosen such that the photon flux emitted by the devices into the $\pm 10^\circ$ cone at the start of the test was $3 \times 10^{16} \text{ photons/cm}^2/\text{s}$ (Figure 4 and Figure S8, Supporting Information). Ultimately, in a microdisplay-type array of high-brightness OLEDs, it is estimated that only a fraction—approximately 20%—of the OLEDs will be operated at the same time, thus we chose a duty cycle of 20%. These driving conditions were further informed by existing studies on light-triggering of ChrimsonR-tdT-expressing RGCs and their recovery kinetics, and are comparable to the conditions used in the LED-DMD-based prosthetics employed in current clinical trials.^[14,19]

To analyze our data, the following stretched exponential function was fitted to the decay of the optical power density over time

$$\frac{I}{I_0} = \exp\left[-\left(\frac{t}{\tau}\right)^\beta\right] \quad (1)$$

with the time constant τ and the dispersion factor β expressing the shape of the curve. Stretched exponential fits are widely used to account for defects in devices, including luminescent quenchers, non-radiative recombination centers, and deep charge traps.^[60–62] To further quantify the useful device lifetime, we quote T_{50} , i.e., the time after which the optical power density has decayed to half of its original value.

For the single-stack $2 \times 2 \text{ mm}^2$ device, the optical power density initially increases, reaching a maximum after 20 min

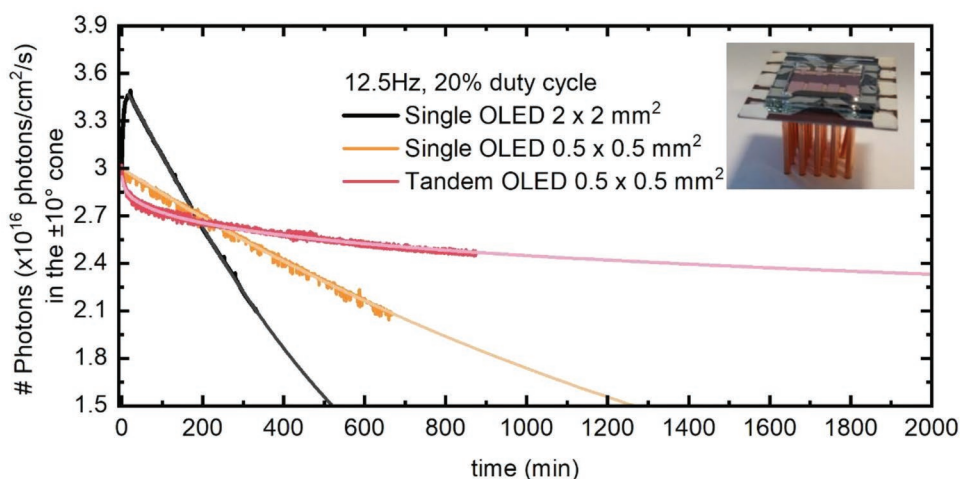


Figure 4. Stability measurements for the single-stack $2 \times 2 \text{ mm}^2$ (black) and $0.5 \times 0.5 \text{ mm}^2$ (orange) devices and the $0.5 \times 0.5 \text{ mm}^2$ tandem device (red) under operation with fixed voltage pulses (12.5 Hz, 20% duty cycle) at an initial photon density of $3 \times 10^{16} \text{ photons/cm}^2/\text{s}$ in the $\pm 10^\circ$ cone. Fits with a stretched exponential decay function (bright colors) reveal a T_{50} of 1246 min ($\approx 21 \text{ h}$) for the single $0.5 \times 0.5 \text{ mm}^2$ device and 800 h for the $0.5 \times 0.5 \text{ mm}^2$ tandem device. The inset shows an image of the silicon substrate with the differently sized OLED devices and copper heat sink.

of pulsed operation, followed by a relatively rapid decay in device brightness ($T_{50} < 500$ min). The optical power density of the smaller 0.5×0.5 mm² device can be fully described by the stretched exponential, i.e., an initial increase in brightness is not observed for the 2×2 mm² device. Extrapolation of the brightness decay for this device predicts a T_{50} of 1246 min (≈ 21 h) with $\tau = 1792$ min and $\beta \approx 1$. The difference between the 2×2 mm² and the 0.5×0.5 mm² is most likely due to an improved lateral heat dissipation as indicated by Figure S9 (Supporting Information).

The tandem-stack device exhibits a steep reduction in brightness within the first 100 min; however, the brightness of this device subsequently decays much more slowly than the single-stack design. T_{50} was calculated to be 48114 min (≈ 800 h), with $\tau = 152511$ and $\beta = 0.32$, for this device. We assume that this very substantially improved stability relative to the single-stack device results from the two-fold higher EQE of the tandem stack at low current levels and the substantially reduced EQE roll-off. In combination, these two factors lead to a more than twofold reduction in the current density when operating at the required photon density of 3×10^{16} photons/cm²/s in the $\pm 10^\circ$ cone, and therefore likely confer a significant reduction in Joule heating.

The use of a small pixel area and pulsed operation result in promising device stability, especially when considering exceptionally high brightness operation (for our orange-emitting OLED, an optical power density of 0.1 mW mm⁻² emitted into the $\pm 10^\circ$ cone corresponds to a luminance of approximately $368\,000$ cd m⁻²). Without the use of a heat sink and when applying constant-current driving conditions, one would expect lifetimes of less than 1 h for such high brightness based on previous literature reports (Figure S10, Supporting Information).^[59,61,63] Driving the OLEDs at an even higher frequency could further enhance the stability of the devices, and still evoke a signal in genetically modified RGCs.^[64] In addition to the advantage of pulsed operation in terms of improving device lifetime, the size of each pixel in the array will be much smaller than for our test devices, which means less power is required and their lifetime is potentially prolonged. In this context, it is important to remember that a visual prosthetic is likely to be operated for only a few hours per day to avoid risk of photodamage to the retina.^[19,20]

3. Discussion

In this study, OLEDs were adjusted to meet the requirements for optical stimulation of genetically modified RGCs through a front-of-eye device. Due to geometric constraints, only the emission into the $\pm 10^\circ$ forward cone of the OLED is usable for this application. Through careful optimization of its MC structure, an orange top-emitting phosphorescent p-i-n OLED stack was optimized to maximize the emission into this cone and to tune the peak emission wavelength to around 600 nm. Driving single-stack OLEDs at 10 V resulted in luminance of $368\,000$ cd m⁻² and a corresponding total optical power density of 1.0 mW mm⁻². Due to the optimized emission profile, 10% of this optical power, i.e., 0.1 mW mm⁻², corresponding to a photon flux of 3×10^{16} photons/cm²/s, is available in the $\pm 10^\circ$

emission cone. These values have previously been reported to enable robust optical stimulation of genetically modified RGCs, without reaching the threshold for tissue damage in the human eye.^[2,11,16,19]

In a further optimization, we demonstrated tandem-stack OLEDs that achieved a maximum luminance of $1\,152\,000$ cd m⁻² in pulsed operation mode; to the best of our knowledge, this is the highest reported luminance for orange phosphorescent p-i-n OLEDs.^[65] The tandem-stack OLEDs exhibit an increased EQE and reduced EQE roll-off, and require lower current densities but higher driving voltages to achieve the same brightness as single-stack OLEDs. We then compared the stability of the single- and tandem-stack devices in pulsed operation mode at the high photon flux of 3×10^{16} photons/cm²/s required for optical stimulation of RGCs. This test revealed that the reduced current density and the presence of two EMLs in the tandem devices very significantly increase the operational lifetime compared to the single-stack architecture, with the tandem stack achieving a T_{50} of 800 h at an initial optical power density of 0.1 mW mm⁻² in the $\pm 10^\circ$ cone. Thus, our tandem design meets both the stability and brightness requirements for front-of-eye prosthetics to optically stimulate genetically modified RGCs in the retina. Compared to devices based on LEDs and DMDs, OLEDs exhibit the potential for color tuning, allow a more straightforward and more highly integrated fabrication process, and possess a planar structure that requires fewer bulky optical components.

4. Experimental Section

Device Fabrication: The OLEDs were fabricated on <111> silicon substrates with a thickness of 500 μ m, which were cleaned in ultrasonic baths with acetone and isopropanol. The substrates were dried with nitrogen, subjected to ultraviolet ozone plasma treatment (3 min), and then placed into a high-vacuum chamber for deposition of the OLEDs via thermal evaporation (base pressure $\approx 10^{-7}$ mbar). Evaporation rates and thicknesses were monitored using a quartz crystal balance, and various shadow masks were used for deposition of the organic layers and the metal electrodes to define the structure and geometry of the active area. The organic materials 2,2',7,7'-tetra(N,N-di-p-tolyl)amino-9,9-spirobifluorene (Spiro-TTB), 2,2'-(perfluoronaphthalene-2,6-diylidene) dimalononitrile (F₆TNAP), N,N'-bis(naphthalen-1-yl)-N,N'-bis(phenyl)-benzidine (NPB), bis(2-methylbenzo-[f,h]quinoxaline)(acetylacetonate) iridium(III) (Ir(MDQ)₂acac), bis(2-methyl-8-quinolinolate)-4-(phenylphenolato)aluminum (BALq), and 4,7-diphenyl-1,10-phenanthroline (BPhen) were purchased from Lumtec and used without further purification. After thermal evaporation, the devices were transferred from the vacuum chamber into a nitrogen-filled glovebox without intermittent exposure to air, and then encapsulated with getter-embedded cavity glass lids attached using a UV-curable epoxy glue. Alphacool GPU RAM Copper heatsinks (14 \times 14 mm) were attached onto the backside of the silicon substrates using Alphacool Eisfrost Xtreme fluid metal paste.

Device Characterization: Characterization of the OLEDs was performed as described by Archer et al.,^[44] measuring angular emission characteristics of the devices with a goniometer and taking deviations from Lambertian characteristics into account when computing optical power density and EQE.

For the voltage-current/voltage-luminance scans in pulsed mode without a heat sink, 10 pulses were applied at each voltage with a 10% duty cycle at 10 Hz (i.e., 10 ms ON every 100 ms), starting from 5 V for the single stack and starting from 10 V for the tandem stack devices. The stability measurements were conducted at 12.5 Hz and 20% duty (16 ms ON every 80 ms).

Supporting Information

Supporting Information is available from the Wiley Online Library or from the author.

Acknowledgements

This research was financially supported by the EPSRC NSF-CBET lead agency agreement (EP/R010595/1, 1706207), the DARPA NESD program (N66001-17-C-4012), the Leverhulme Trust (RPG-2017-231), and the Alexander von Humboldt Stiftung (Humboldt-Professorship to M.C.G.). C.K. acknowledges support from the Basic Science Research Program through the National Research Foundation of Korea (NRF), funded by the Ministry of Education (2017R1A6A3A03012331). Y.D. acknowledges a stipend from the Chinese Scholarship Council (CSC).

Conflict of Interest

The authors declare no conflict of interest.

Data Availability Statement

The data that support the findings of this study are openly available on the St Andrews University repository under <https://doi.org/10.17630/a03d2274-22bb-4101-80cd-f80281ecc807>.

Keywords

channelrhodopsins, neurophotronics, organic electronics, photostimulation, retinitis pigmentosa

Received: April 14, 2022
Revised: July 14, 2022
Published online:

- [1] E. Zrenner, K. U. Bartz-Schmidt, H. Benav, D. Besch, A. Bruckmann, V.-P. Gabel, F. Gekeler, U. Greppmaier, A. Harscher, S. Kibbel, J. Koch, A. Kusnyerik, T. Peters, K. Stingl, H. Sachs, A. Stett, P. Szurman, B. Wilhelm, R. Wilke, *Proc. R. Soc. B* **2011**, 278, 1489.
- [2] A. Sengupta, A. Chaffiol, E. Macé, R. Caplette, M. Desrosiers, M. Lampič, V. Forster, V. B. Mahajan, J. Y. Lin, J. Sahel, S. Picaud, D. Dalkara, J. Duebel, *EMBO Mol. Med.* **2016**, 8, 1248.
- [3] A. Farnum, G. Pelled, *Front. Neurosci.* **2020**, 14, 36.
- [4] S. Russell, J. Bennett, J. A. Wellman, D. C. Chung, Z.-F. Yu, A. Tillman, J. Wittes, J. Pappas, O. Elci, S. McCague, D. Cross, K. A. Marshall, J. Walshire, T. L. Kehoe, H. Reichert, M. Davis, L. Raffini, L. A. George, F. P. Hudson, L. Dingfield, X. Zhu, J. A. Haller, E. H. Sohn, V. B. Mahajan, W. Pfeifer, M. Weckmann, C. Johnson, D. Gewaily, A. Drack, E. Stone, et al., *Lancet* **2017**, 390, 849.
- [5] J. Bennett, *Mol. Ther.* **2017**, 25, 1076.
- [6] T. H. Kim, Y. Zhang, J. Lecoq, J. C. Jung, J. Li, H. Zeng, C. M. Niell, M. J. Schnitzer, *Cell Rep.* **2016**, 17, 3385.
- [7] P. R. Roelfsema, D. Denys, P. C. Klink, *Trends Cognit. Sci.* **2018**, 22, 598.
- [8] J. Joshi, M. Rubart, W. Zhu, *Front. Bioeng. Biotechnol.* **2020**, 7, 466.
- [9] S. P. Daiger, *Arch. Ophthalmol.* **2007**, 125, 151.
- [10] V. Busskamp, S. Picaud, J. A. Sahel, B. Roska, *Gene Ther.* **2012**, 19, 169.
- [11] P. Degenaar, N. Grossman, M. A. Memon, J. Burrone, M. Dawson, E. Drakakis, M. Neil, K. Nikolic, *J. Neural Eng.* **2009**, 6, 035007.
- [12] P. S. Lagali, D. Balya, G. B. Awatramani, T. A. Münch, D. S. Kim, V. Busskamp, C. L. Cepko, B. Roska, *Nat. Neurosci.* **2008**, 11, 667.
- [13] X. Duan, G. Nagel, S. Gao, *Appl. Sci.* **2019**, 9, 664.
- [14] A. Morton, C. Murawski, Y. Deng, C. Keum, G. B. Miles, J. A. Tello, M. C. Gather, *Adv. Biosyst.* **2019**, 3, 1800290.
- [15] C. Murawski, A. Mischok, J. Booth, J. D. Kumar, E. Archer, L. Tropf, C. Keum, Y. Deng, K. Yoshida, I. D. W. Samuel, M. Schubert, S. R. Pulver, M. C. Gather, *Adv. Mater.* **2019**, 31, 1903599.
- [16] International Commission on Non-Ionizing Radiation Protection (ICNIRP) Guidelines, Health Physics Society, **1997**, <https://www.icnirp.org/cms/upload/publications/ICNIRPbroadband.pdf>.
- [17] B. Yan, M. Vakulenko, S.-H. Min, W. W. Hauswirth, S. Nirenberg, *Vision Res.* **2016**, 121, 57.
- [18] N. C. Klapoetke, Y. Murata, S. S. Kim, S. R. Pulver, A. Birdsey-Benson, Y. K. Cho, T. K. Morimoto, A. S. Chuong, E. J. Carpenter, Z. Tian, J. Wang, Y. Xie, Z. Yan, Y. Zhang, B. Y. Chow, B. Surek, M. Melkonian, V. Jayaraman, M. Constantine-Paton, G. K.-S. Wong, E. S. Boyden, *Nat. Methods* **2014**, 11, 338.
- [19] G. Gauvain, H. Akolkar, A. Chaffiol, F. Arcizet, M. A. Khoei, M. Desrosiers, C. Jaillard, R. Caplette, O. Marre, S. Bertin, C.-M. Fovet, J. Demilly, V. Forster, E. Brazhnikova, P. Hantraye, P. Pouget, A. Douar, D. Pruneau, J. Chavas, J.-A. Sahel, D. Dalkara, J. Duebel, R. Benosman, S. Picaud, *Commun. Biol.* **2021**, 4, 125.
- [20] J.-A. Sahel, E. Boulanger-Scemama, C. Pagot, A. Arleo, F. Galluppi, J. N. Martel, S. D. Esposti, A. Delaux, J.-B. de Saint Aubert, C. de Montleau, E. Gutman, I. Audo, J. Duebel, S. Picaud, D. Dalkara, L. Blouin, M. Tiel, B. Roska, *Nat. Med.* **2021**, 27, 1223.
- [21] F. Galluppi, D. Pruneau, J. Chavas, X. Lagorce, C. Posch, G. Chenegros, G. Cordurie, C. Galle, N. Oddo, R. Benosman, in *Proceedings of the 2017 IEEE Int. Symp. on Circuits and Systems (ISCAS)*, IEEE, Piscataway, NJ **2017**, pp. 1–4.
- [22] L. Sileo, S. H. Bitzenhofer, B. Spagnolo, J. A. Pöppel, T. Holzhammer, M. Pisanello, F. Pisano, E. Bellistri, E. Maglie, M. De Vittorio, P. Ruther, I. L. Hanganu-Opatz, F. Pisanello, *Front. Neurosci.* **2018**, 12, 771.
- [23] N. McAlinden, Y. Cheng, R. Scharf, E. Xie, E. Gu, C. F. Reiche, R. Sharma, P. Tathireddy, M. D. Dawson, L. Rieth, S. Blair, K. Mathieson, *Neurophotonics* **2019**, 6, 035010.
- [24] M. Vigier, T. Pilloix, B. Dupont, G. Moritz, in *2020 IEEE 63rd Int. Midwest Symp. on Circuits and Systems (MWSCAS)*, IEEE, Piscataway, NJ **2020**, pp. 876–879.
- [25] E. Quesnel, A. Lagrange, M. Vigier, M. Consonni, M. Tournaire, V. Le Marchand, A. Suhm, P. Demars, J. Pillet, B. Ben Bakir, N. Olivier, E. Feltin, J. M. Lamy, M. D'Amico, E. Cao, G. Haas, L. Charrier, P. Coni, *J. Soc. Inf. Disp.* **2021**, 29, 3.
- [26] M. S. White, M. Kaltenbrunner, E. D. Głowacki, K. Gutnichenko, G. Kettlgruber, I. Graz, S. Aazou, C. Ulbricht, D. A. M. Egbe, M. C. Miron, Z. Major, M. C. Scharber, T. Sekitani, T. Someya, S. Bauer, N. S. Sariciftci, *Nat. Photonics* **2013**, 7, 811.
- [27] J. Liang, L. Li, X. Niu, Z. Yu, Q. Pei, *Nat. Photonics* **2013**, 7, 817.
- [28] K. Yoshida, P. P. Manousiadis, R. Bian, Z. Chen, C. Murawski, M. C. Gather, H. Haas, G. A. Turnbull, I. D. W. Samuel, *Nat. Commun.* **2020**, 11, 1171.
- [29] T. Fujii, C. Kon, Y. Motoyama, K. Shimizu, T. Shimayama, T. Yamazaki, T. Kato, S. Sakai, K. Hashikaki, K. Tanaka, Y. Nakano, *J. Soc. Inf. Disp.* **2018**, 26, 178.
- [30] A. Steude, E. C. Witts, G. B. Miles, M. C. Gather, *Sci. Adv.* **2016**, 2, e1600061.
- [31] C. M. Lochner, Y. Khan, A. Pierre, A. C. Arias, *Nat. Commun.* **2014**, 5, 5745.
- [32] A. K. Bansal, S. Hou, O. Kulyk, E. M. Bowman, I. D. W. Samuel, *Adv. Mater.* **2015**, 27, 7638.

- [33] H. Lee, E. Kim, Y. Lee, H. Kim, J. Lee, M. Kim, H.-J. Yoo, S. Yoo, *Sci. Adv.* **2018**, 4, eaas9530.
- [34] C. Lian, M. Piksa, K. Yoshida, S. Persheyev, K. J. Pawlik, K. Matczyszyn, I. D. W. Samuel, *npj Flexible Electron.* **2019**, 3, 18.
- [35] S. Hofmann, M. Thomschke, P. Freitag, M. Furno, B. Lüssem, K. Leo, *Appl. Phys. Lett.* **2010**, 97, 253308.
- [36] N. C. Giebink, S. R. Forrest, *Phys. Rev. B* **2008**, 77, 235215.
- [37] C. Murawski, K. Leo, M. C. Gather, *Adv. Mater.* **2013**, 25, 6801.
- [38] C. Murawski, P. Liehm, K. Leo, M. C. Gather, *Adv. Funct. Mater.* **2014**, 24, 1117.
- [39] C. Keum, C. Murawski, E. Archer, S. Kwon, A. Mischok, M. C. Gather, *Nat. Commun.* **2020**, 11, 6250.
- [40] Y. Deng, C. Keum, S. Hillebrandt, C. Murawski, M. C. Gather, *Adv. Opt. Mater.* **2020**, 9, 2001642.
- [41] M. Furno, R. Meerheim, S. Hofmann, B. Lüssem, K. Leo, *Phys. Rev. B* **2012**, 85, 115205.
- [42] X. Fu, Y. Mehta, Y. Chen, L. Lei, L. Zhu, N. Barange, Q. Dong, S. Yin, J. Mendes, S. He, R. Gogusetti, C. Chang, F. So, *Adv. Mater.* **2021**, 33, 2006801.
- [43] T. Schwab, C. Fuchs, R. Scholz, A. Zakhidov, K. Leo, M. C. Gather, *Opt. Express* **2014**, 22, 7524.
- [44] E. Archer, S. Hillebrandt, C. Keum, C. Murawski, J. Murawski, F. Tenopala-Carmona, M. C. Gather, *Adv. Opt. Mater.* **2020**, 9, 2000838.
- [45] P. Cusumano, *Synth. Met.* **2003**, 139, 657.
- [46] K.-Y. Lee, P. C.-P. Chao, *IEEE Trans. Electron Devices* **2012**, 59, 1123.
- [47] X. Li, X.-A. Cao, *Org. Electron.* **2013**, 14, 2523.
- [48] J. M. Park, in *EKC2008 Proc. of the EU-Korea Conf. on Science and Technology* (Ed: S.-D. Yoo), Springer, Berlin **2008**, pp. 383–391.
- [49] C.-Y. Lin, Y.-L. Chiu, in *Proceedings of the 2017 Int. Conf. on Intelligent Informatics and Biomedical Sciences (ICIIBMS)*, IEEE, Piscataway, NJ **2017**, pp. 223–224.
- [50] V. Ningaraju, H.-C. Lin, P.-A. Chen, K.-L. Lin, *Solid State Electron. Lett.* **2019**, 1, 119.
- [51] M. A. Baldo, C. Adachi, S. R. Forrest, *Phys. Rev. B* **2000**, 62, 10967.
- [52] S. Scholz, D. Kondakov, B. Lüssem, K. Leo, *Chem. Rev.* **2015**, 115, 8449.
- [53] M. Ishii, Y. Taga, *Appl. Phys. Lett.* **2002**, 80, 3430.
- [54] T. Xu, J.-G. Zhou, C.-C. Huang, L. Zhang, M.-K. Fung, I. Murtaza, H. Meng, L.-S. Liao, *ACS Appl. Mater. Interfaces* **2017**, 9, 10955.
- [55] H. Kanno, R. J. Holmes, Y. Sun, S. Kena-Cohen, S. R. Forrest, *Adv. Mater.* **2006**, 18, 339.
- [56] A. Cester, D. Bari, J. Framarin, N. Wrachien, G. Meneghesso, S. Xia, V. Adamovich, J. J. Brown, *Microelectron. Reliab.* **2010**, 50, 1866.
- [57] S. H. Choi, T. I. Lee, H. K. Baik, H. H. Roh, O. Kwon, D. hak Suh, *Appl. Phys. Lett.* **2008**, 93, 183301.
- [58] K. Kwak, K. Cho, S. Kim, *Opt. Express* **2013**, 21, 29558.
- [59] R. Meerheim, S. Scholz, S. Olthof, G. Schwartz, S. Reineke, K. Walzer, K. Leo, *J. Appl. Phys.* **2008**, 104, 014510.
- [60] C. Féry, B. Racine, D. Vaufrey, H. Doyeux, S. Cinà, *Appl. Phys. Lett.* **2005**, 87, 213502.
- [61] M. C. Gather, S. Köber, S. Heun, K. Meerholz, *J. Appl. Phys.* **2009**, 106, 024506.
- [62] R. Meerheim, K. Walzer, M. Pfeiffer, K. Leo, *Appl. Phys. Lett.* **2006**, 89, 061111.
- [63] S. Chung, J.-H. Lee, J. Jeong, J.-J. Kim, Y. Hong, *Appl. Phys. Lett.* **2009**, 94, 253302.
- [64] T. Mager, D. Lopez de la Morena, V. Senn, J. Schlotte, A. D'Errico, K. Feldbauer, C. Wrobel, S. Jung, K. Bodensiek, V. Rankovic, L. Browne, A. Huet, J. Jüttner, P. G. Wood, J. J. Letzkus, T. Moser, E. Bamberg, *Nat. Commun.* **2018**, 9, 1750.
- [65] R. Cui, L. Zhou, Y. Jiang, Y. Wang, Y. Li, X. Zhao, L. Lu, *Dyes Pigm.* **2020**, 178, 108311.